**Fermi National Accelerator Laboratory**

# Jet Energy Measurement CDF Experience*

John Huth
Fermi National Accelerator Laboratory
P.O. Box 500, Batavia, Illinois 60510 U.S.A.

March 1989

# Jet Energy Measurement

## CDF Experience

John Huth

MS 318

Fermi National Accelerator Laboratory

Box 500

Batavia IL 60510

## 1  Introduction

This paper outlines CDF experience with jet energy measurements, with an emphasis on the systematic uncertainties. The systematics can be broadly classified as a) the low energy response (e/h), b) fragmentation, c) clustering effects, d) the detector simulation, e) calibration and f) the underlying event. In addition, for specific measurements, like the inclusive $E_t$ distribution, the existence of a steeply falling spectrum, convolved with a wide resolution function can give a distorted result. Resolution, therefore will also be discussed.

## 2  The CDF detector

The CDF detector is described in detail in a series of NIM articles [1]. The calorimeters consist of three discrete systems, segmented in pseudorapidity ($\eta$), which is related to the polar angle by the expression, $\eta \equiv log_e(cot(\theta/2))$. Figure 1 shows a cross section of the CDF detector. The calorimetry consists of a central ($|\eta| \leq 1.1$), a plug ($1.1 \leq |\eta| \leq 2.7$) and a forward ($2.7 \leq |\eta| \leq 4.2$) calorimeter. The forward and plug are gas calorimeters consisting of
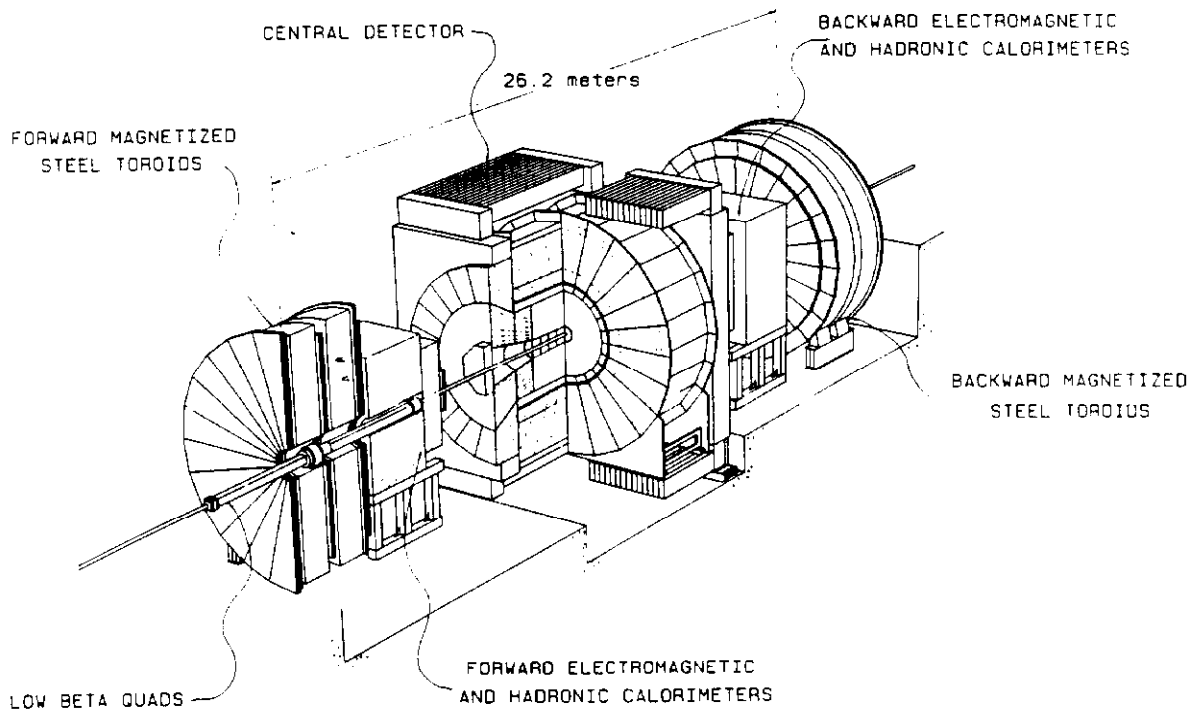
Figure 1: Cutaway view of the CDF detector.

proportional tubes overlaying cathode pads. The central calorimeter is a scintillator calorimeter.

A projective tower geometry is used throughout CDF, with a segmentation of 0.1 units in pseudorapidity for all calorimeters and 15° in azimuth ($\phi$) for the central, and 5° for the gas calorimeters. Major transitions between detectors result in *cracks* at 90°, 30° and 10° in polar angle. The influence of these transition regions are examined in detail later on in the paper.

The EM compartment of the central calorimeter [2] consists of 17 $\lambda_r$ of a lead scintillator sandwich. Each scintillator is read out by two wavelength shifters, each connected to a pair of phototubes via lightguides. The hadron compartment consists of 4.5 interaction lengths of an iron scintillator sandwich. The scintillator is also read out with wavelength shifters.

The energy scale for the EM calorimeter was defined using 50 GeV electrons centered on the face of the calorimeter tower. The peak of the pulse height distribution for the central EM compartment defines the energy scale at 50 GeV. The energy scale for the hadron compartment was set using the response of 50 GeV pions which exhibited less that 400 MeV (minimum ionizing) in the EM calorimeter. For these pions, the peak in the central hadron

compartment is used to define the energy scale. The energy reported in the calorimeters is taken to be the sum of the energies reported in the EM and hadronic compartments.

A set of vertex time projection chambers (VTPC), surrounding the beampipe, are used for determination of the event vertex position along the beamline It also provides an identification of bunch crossings containing multiple $\bar{p}p$ interactions. The central tracking chamber (CTC) is an 84 layer axial wire chamber inside a 1.5 T magnetic field. Track coordinates along the beamline are determined from a 3° stereo projection. The momentum resolution of the CTC is approximately $\delta p/p^2 = 0.002$ for tracks with greater than 2 GeV of transverse momentum. The CTC was used to help determine the low energy response of the central calorimeter, to measure the fragmentation properties of jets and to help in the rejection of backgrounds generated by cosmic ray interactions. This paper will concentrate on data collected with the central calorimeter, and the use the central tracking chamber for both fragmentation measurements and the determination of the low energy response of the calorimeter.

# 3  The Inclusive Cross Section

The measurement of the inclusive jet cross section, $p\bar{p} \rightarrow$ Jet $+$ **X** , is a typical analysis which both illustrates the systematic effects in jet energy measurement, and gives some indication of the ability to make meaningful physics measurements in a real detector. The spectrum of the jet cross section, $d\sigma/dE_t$, is sensitive not only to next to leading order QCD processes, but also to possible quark substructure [3], and the production of massive particles with strong couplings, such as axigluons [4]. Figure 3 shows typical Feynman graphs associated with both QCD and possible quark substructure. The dominant QCD graphs involve a t-channel exchange of gluons. The existence of a quark substructure is typically parameterized by the addition of a contact term to the QCD Lagrangian of the form [3]:

$$\mathcal{L}_{\text{int}} = \eta_o \frac{g^2}{2\Lambda_c}(\bar{q}\gamma^\mu q)^2 \tag{1}$$

Here $\eta_o$ is $\pm 1$, representing the phase of the interaction, giving constructive or destructive interference with QCD. Although there are many plausible forms,
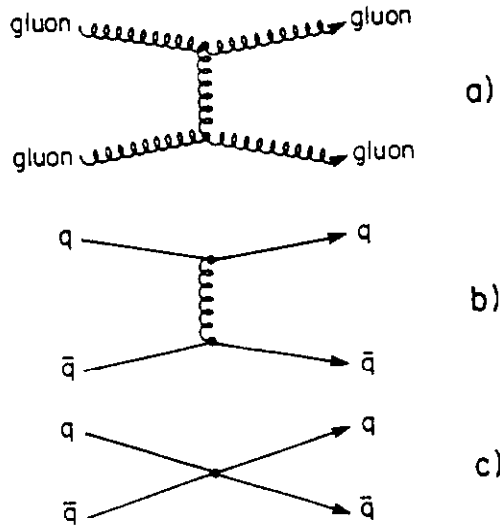
3

Figure 2: Typical leading order graphs which contribute to 2 jet final states. At low energy, gluon-gluon scattering dominates, at high energy quark-antiquark scattering dominates. For both processes, t-channel exchange is the largest process. The contact term at the bottom is used to parameterize the effect of a quark substructure.

the isoscalar, color singlet interaction, with $g^2 = 4\pi$ is typically chosen as a convenient reference. The existence of this term, characterized by a coupling with the units of (energy)$^{-1}$, is to increase the jet cross section over that predicted by QCD at high energies. At sufficiently large $E_t$, the $\mathcal{L}_{int}$ term dominates the cross section, which will rise with $\hat{s}$. Higher order corrections to the two parton final state exist for gluons only at the moment, and soon one expects to obtain the full calculation at next to leading order [6].

# 4  Clustering Jets

The first step in measuring jet cross sections is identifying jets in calorimeter data. One takes an operational definition for jets as being the hadronic remnants of single quark. The hadronic remnants have a typical limited momentum transverse to the outgoing parton line. This transverse momentum is typically 200 to 500 MeV. As a consequence of the limited momentum transverse to the central axis, jets with energies below 10 GeV are poorly
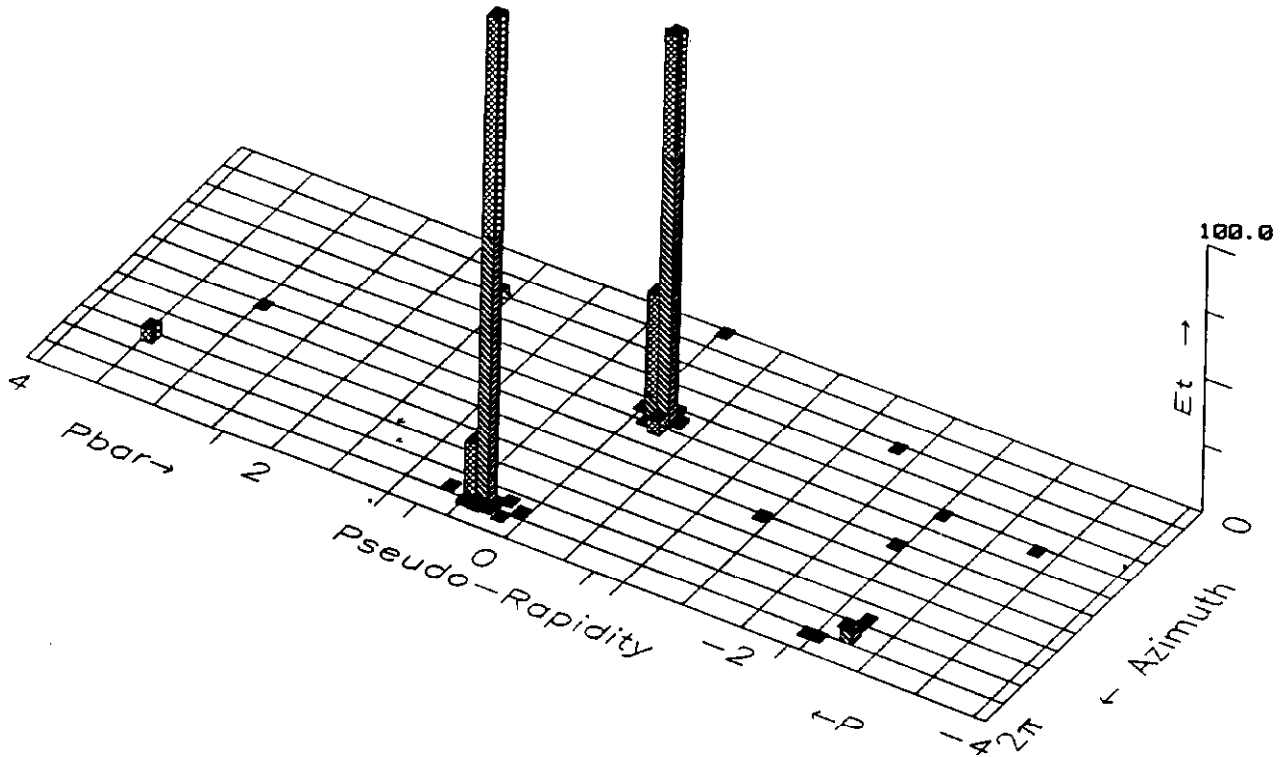
Figure 3: One of the highest $E_t$ jet events seen at the CDF detector, with an invariant mass of approximately 630 GeV.

defined; only above 15 GeV one begins to have some confidence in clustering as a means of jet identification. Figure 4 shows a typical two jet event at the highest transverse energies seen at CDF. The existence of clusters of energy in the $\eta - \phi$ plot is unmistakeable. Figure 4 shows a typical four jet event. In this figure the jet energies range from 40 to 60 GeV, and, although still clearly identifiable as isolated clusters, it is clear that they are substantially broader in extent than the jets in figure 4.

The identification of jets is done using a clustering algorithm based on calorimeter data in which one seeks to identify separated clusters of energy. Four algorithms have been evaluated for their ability to find clusters in dense events. The two most commonly used algorithms will be termed the *nearest neighbor* and the *fixed cone* algorithms. The nearest neighbor algorithm uses a seed tower above a threshold (2 GeV), and finds all contiguous towers surrounding the seed tower with energies above a shoulder threshold (0.2 GeV). The 8 nearest neighbors of the seed tower are examined. To be *merged* (*ie* energy added into the cluster) , the neighbor tower must have an $E_t$ less than $f \times Et_{seed}$, where $f$, referred to the as the parent daughter ratio, is a
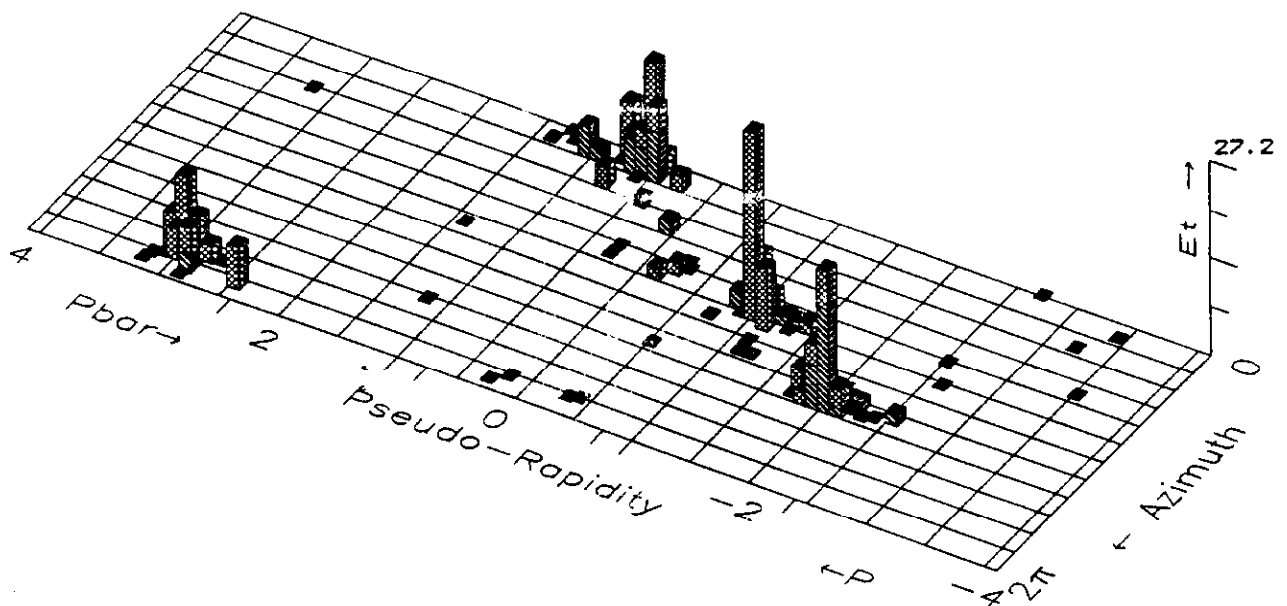
Figure 4: A four jet event as seen in the CDF detector. All 4 jets have $E_t$'s in excess of 40 GeV.

fixed fraction, set to 2.0 by default. The merged towers are themselves used as seeds for a search of contiguous towers. The parent-daughter test allows jets to be defined around local maxima in the transverse energy. If a tower is not merged, it becomes the seed of another cluster.

The cone algorithm starts from the clusters defined in the contiguous tower algorithm before the merging step, and uses the $E_t$ weighted centroid as the center of a circle (or cone) in $\eta - \phi$ space, with a radius $\Delta R = \sqrt{\Delta\eta^2 + \Delta\phi^2}$. All the towers above the shoulder threshold inside this circle are included in the cluster. The centroid is recomputed from these towers, a new circle is drawn and a new list of towers is generated. This process is iterated until the list of towers inside the cone is stable upon successive iterations. The fixed cone algorithm has the advantage that it is most closely related to the algorithms used by theorists to regulate collinear ingularities in the calculation of gluon *bremsstrahlung* [5],[6].

The two other algorithms which we have investigated are the $E_t$ dependent cone algorithm which is similar to the fixed cone algorithm, but has a

cone radius that varies as:

$$\Delta R = Min(\frac{12.0}{E_t}, 0.6).$$ (2)

This is based on the notion that a jet is a collection of particles with a limited energy transverse to a central axis, and thus the effective size would be related to the jet $E_t$. Because of the presence of gluon *bremstrahlung* , jets can broaden at higher $E_t$, complicating matters.

Finally there is the pairwise merging algorithm which starts with the clusters from the nearest neighbor algorithm and and then tries to pair them, based on which pair are the closest in $\eta - \phi$ space. The process continues until all towers within some minimum distance are merged together.

A number of tests were developed to measure the performance of the algorithms. The main test is to take a sample of events that are considered clean, two jet events, in which the leading two jets are approximately back-to-back in azimuth and there are no other jets in the event above a stringent threshold (typically 5 GeV). The towers from these two events are merged together, and the clustering algorithm is then run on the merged event. We can find the fraction of the time that clusters are merged together as a function of the separation of the clusters. This is shown in figure 5. The sharpness of the cutoff in $\eta - \phi$ space is a measure used to evaluate the algorithms. In particular the fixed cone algorithm gives the best performance because of the relative sharpness of the cutoff.

From the same merging test, one also can ask how much energy is shuffled between nearby clusters which are themselves not merged. For all unmerged clusters in the merged events, one can calculate the difference in the $E_t$ reported in the unmerged versus the merged events. This difference is shown in figure 6 for the different algorithms. Again it is clear that the most stable algorithms from this test are the fixed cone algorithms. CDF has chosen the fixed cone algorithm both because of its stability and because of the close correspondence to the way that cutoffs are imposed in QCD calculations [6]. From a theoretical standpoint the nearest neighbor algorithm is more difficult to work with.
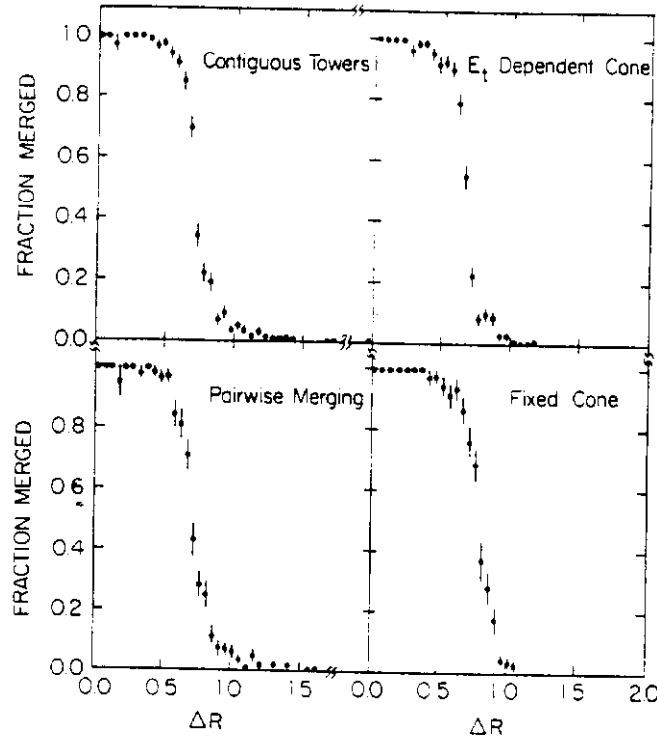
Figure 5: The cluster merging function. This is defined as the fraction of the time a pair of clusters from independent two jet events are found as a single cluster when the tower energies from both events are added together and the clustering algorithm is re-applied. This is shown as a function of the separation in $\eta - \phi$ space.
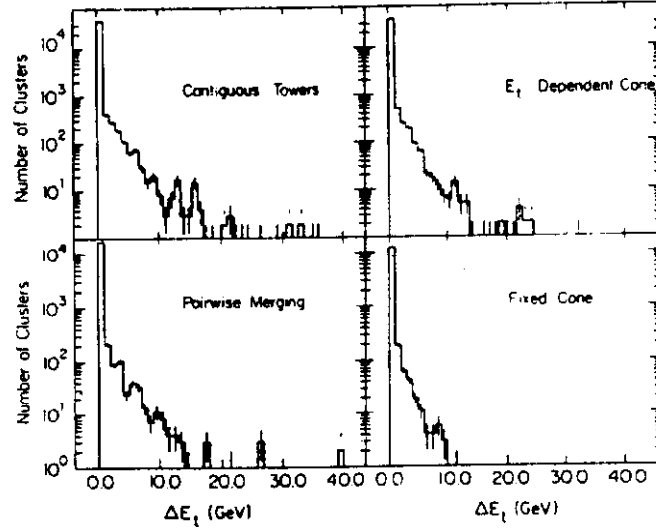


Figure 6: Difference in transverse energy for clusters in unmerged events minus the energy for the same clusters when overlaid on other dijets events, but the clusters are still found as separate. The fixed cone algorithm appears to have the least sharing of energy.

# 5   Energy Corrections

The CDF calorimeter is non-compensating, meaning that the calorimeter will report different energies for pions than for electrons or photons; this difference is a function of the energy of the incident particle [7]. The calorimeter cells are added by taking a sum of the energies reported in the EM and Hadronic compartments. Jets consist of a mixture of charged and neutral particles, which possess a variable fragmentation spectrum. The response of a non-compensating calorimeter to jets is really a convolution of the calorimeter response to electromagnetic and hadronic showers with the fragmentation function for jets. If the calorimeter response is known for both pions and electrons of all energies, and the fragmentation function, for jets are known, then it is possible to determine a correction factor for the reported jet energy. There are thus two pieces of information that are needed to derive the jet energy corrections. First, the calorimeter response to low energy pions must be determined, second the fragmentation function for jets must be measured, or somehow inferred.

## 5.1   Low energy response

The low energy response of the central calorimeter was determined by using a combination of test beam and minimum bias data. Test beam data were taken down to energies of 10 GeV for electrons and pions. The test beam could not run below this energy; isolated tracks in the central tracking chamber in minimum bias events were used to provide an effective low energy test beam. It is important for future experiments to have test beams that can go to low energies. Tracks in minimum bias events were used if they pointed at a central calorimeter tower and were sufficiently isolated. The isolation requirement was that no other tracks pointed into a grid of at least $5 \times 5$ calorimeter towers. The central $3 \times 3$ towers were added up to yield the response.

A systematic uncertainty associated with this technique is the production of neutral particles which may be correlated with higher $p_t$ tracks due to jet-like structure. This background was determined by looking at the ambient background of isolated energy (no tracks in a $5 \times 5$ square), and by comparing it to the rate at which charged pions accompanied selected high
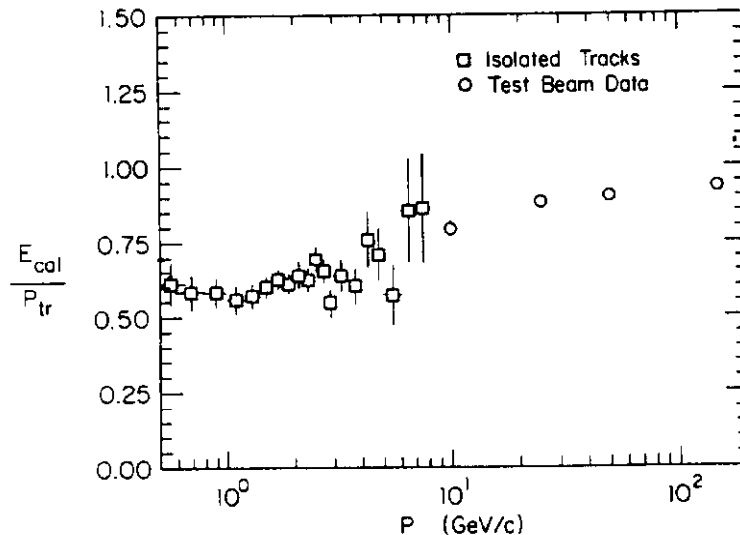
9

Figure 7: The calorimeter response to pions. The response is the ratio of the energy reported in the calorimeter (EM+Hadronic) divided by the energy of the incident particle. The data reported is from test beam pions and from isolated charged particles in minimum bias events. Both systematic and statistical uncertainties are reported.

$p_t$ tracks. From this measurement, a background subtraction is performed, and a response curve derived.

Figure 7 shows the calorimeter response to charged pions from the test beam, and to isolated charged particles in the minimum bias data. The errors reported are a combination of statistical and systematic effects. The systematic uncertainties dominate at the lower end of the spectrum, and come almost entirely from the background subtraction. At high energy, the test beam points are not precisely unity because the pions in fig. 7 are allowed to shower in the EM, whereas the pions in the energy scale determination are chosen if they exhibit minimum ionizing characteristics in the EM compartment. All points represent the average charged pion response in the central calorimeter.

From figure 7 it is apparent that the energy reported by the calorimeter for low energy charged pions can be as low as 65% of the true energy. Depending

on the composition of jets, this can represent a substantial correction.

## 5.2  Fragmentation

In order to determine the effect of the nonlinearities on the calorimeter response to jets, we must first determine the fragmentation properties of the jets. Much data exists on jet fragmentation, predominately from $e^+e^-$ colliders, but some from $p\bar{p}$ collisions [9]. One problem in taking fragmentation functions determined by other experiments is that these data may contain different admixtures of quarks and gluons in the final state, and at different effective $Q^2$ scales. CDF has attempted to measure the jet fragmentation properties, and derive a consistent simulation of the final state properties of jets observed at the Tevatron.

The tracking data were used to measure several distributions describing the final state jets. Only distributions were used which involved only the CTC in order to avoid use of calorimeter data for the tuning. The distributions included the charged particle multiplicity inside a jet cone, the mean momentum transverse to the jet axis and a modified fragmentation function. Normally in deriving the jet fragmentation function, $D(x) \equiv 1/N_{jet}dN_{ch}/dz$, the variable $z$ is the projection of a charged track's momentum along the jet axis, divided by the total jet energy. The integral, $\int D(z)dz$ is the charged multiplicity. However, if the total jet energy is used, the calorimeter energy is coupled into the measurement in a complicated way. To simplify the problem, we chose to measure an effective *charged* fragmentation function, $D(z')$ where $z'$ is the the projected track momentum divided by the total *visible charged* energy in the jet, rather than divided by the calorimeter energy.

The simulation of the jet fragmentation was done using ISAJET V5.2 [8]. ISAJET fragmentation is based on the Feynman Field model [13] and has a large number of tunable parameters. The main parameters that were tuned included the effective gluon mass, the mean $p_t$ with respect to the jet axis, and the coefficients of the Feynman-Field parameterization. Figure 8 shows the average charged multiplicity inside the cone of 0.7 before and after tuning ISAJET.

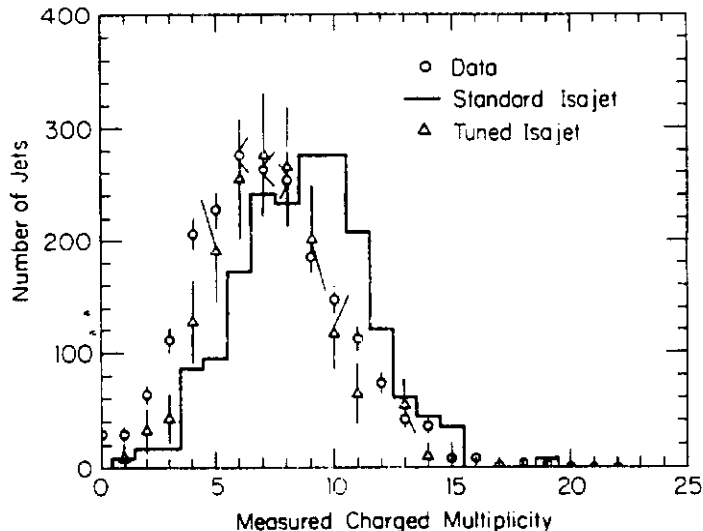The light quark splitting function in the Feynman-Field parameterization

Figure 8: Charged multiplicity distribution for particles in jets. The multiplicity is not corrected for efficiency and only counts particles inside a cone of radius 1.0 in $\eta - \phi$. The solid line is the untuned ISAJET+simulation result, the tuned ISAJET+simulation result is represented by the dotted line, and shows much better agreement with the data.

(as it appears in ISAJET) is:

$$f(z) = 1 - a + a(b+1)(1-z)^b \tag{3}$$

In our tuning we have found that $a = 0.22$ and $b = 2.0$ appears to give the closest correspondence to the data. In addition to tuning the fragmentation distributions, we attempted to set upper and lower limits on the possible fragmentation functions. We determined these from the level of certainty we had on the fragmentation measurement. The upper limit corresponds to the parameters $a = 0.57$ and $b = 2.0$, which is a stiff fragmentation [10]. The lower limit corresponds to the parameters $a = 0.96$ and $b = 3.0$, with a softer fragmentation than observed. From these upper and lower bounds, we were able to determine a systematic uncertainty in the energy scale associated with the soft and hard limits. These uncertainties are the most significant for low $E_t$ jets where the influence of the nonlinearity is the largest. After fragmenting the partons, ISAJET generates a $p_t$ for particles relative to the jet axis, and then rescales energies in the entire event in an attempt to conserve momentum and $\hat{s}$. This rescaling can make the tuning nontrivial,

12

and couples the longitudinal and transverse variables.

## 5.3   Crack Response

*Crack* is a generic term for an uninstrumented region of the calorimeter. In CDF, there is a distinction to be made between two kinds of cracks because of their influence on the analysis. There are cracks in $\phi$ which, for the central detector, represent the boundaries between wedges. There are also cracks in $\eta$ which are more substantial and represent transition regions between different types of calorimeters (*ie.* central and plug, or plug and forward). In early analyses of the inclusive jet cross section, we made fiducial cuts to restrict the jets measured to the central calorimeter. This was largely because the 1987 run had only the central calorimeter fully in the trigger.

### 5.3.1   $\phi$ Cracks

The $\phi$ cracks are effectively integrated over in the determination of the corrections to jet energy. Figure 9 shows a diagram of a $\phi$ crack in the central calorimeter. Because of the crack filling bar of tungsten, at no point will a charged particle actually traverse a region without any absorber material, although the active region does not fully cover the crack area. The tungsten in the crack filler will induce showers of sufficient size to produce a signal in the phototubes.

Test beam data were used as input to simulate the calorimeter response to pions and electrons incident at or near the $\phi$ cracks. This map will then be used in the simulation to estimate the effective loss of energy in the cracks. Figure 10 shows the result of a test beam scan across a $\phi$ crack using 50 GeV pions, also shown is the simulation response. Figure 11 shows a similar plot for the response to test beam electrons scanned across the crack. The bump in the pion response at 0 cm is due to the steel skin of the wedges. Approximately 30% loss is seen in the cracks. There is no single spot where the loss drops to zero because the tungsten bar induces sufficient showering. 8% of the solid angle in the central calorimeter has a region of reduced response due to the $\phi$ cracks.

For the jet energy corrections, the simulation with the tuned jet fragmentation function is used to integrate the response over the $\phi$ cracks. A
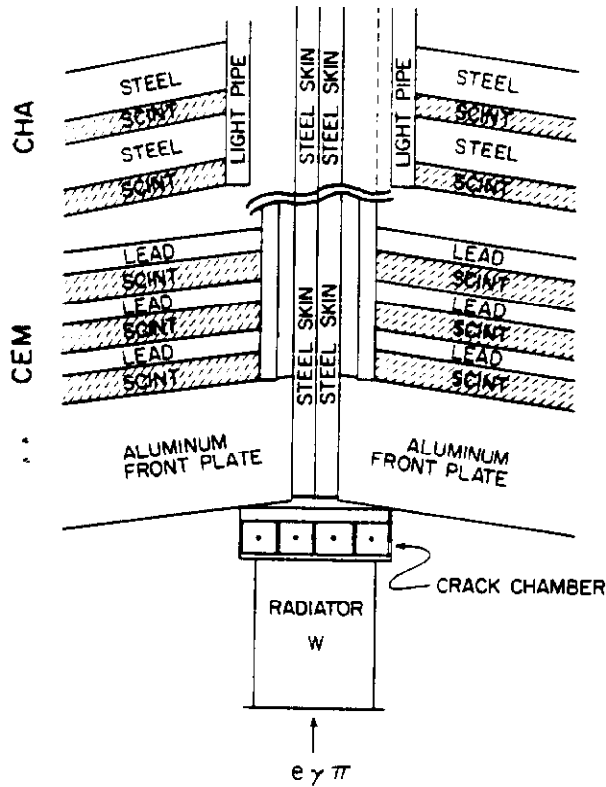
13

Figure 9: Detail of the $\phi$ crack of the central calorimeter. Active scintillator is shown in the cross hatching. A tungsten bar covers the crack so that no charged particle can pass through a region with no absorber.

systematic uncertainty was assigned to the jet energy scale, related to the crack response. This was derived from the change in response of the simulation depending on the treatment of energy appearing in the light guides. When a track hits the light guide of wavelength shifter, a response larger than normal can be produced, and with little sharing with the other phototube. There are corrections for this which assume a single track is incident. In jets, the situation is less clear - for example a track could hit a hot spot and there could also be a track in the center of the tower. By turning on and off the hot spot correction used, the variation in response is a measure of the uncertainty in the crack response. It appears that the uncertainty is roughly energy independent, although there is little data on the crack response in the test beam for other than 50 GeV pions. Work is in progress to understand the energy dependence of the crack response. In principle one could perform jet by jet correction which includes a response map. When this correction was attempted, little improvement in resolution was seen.
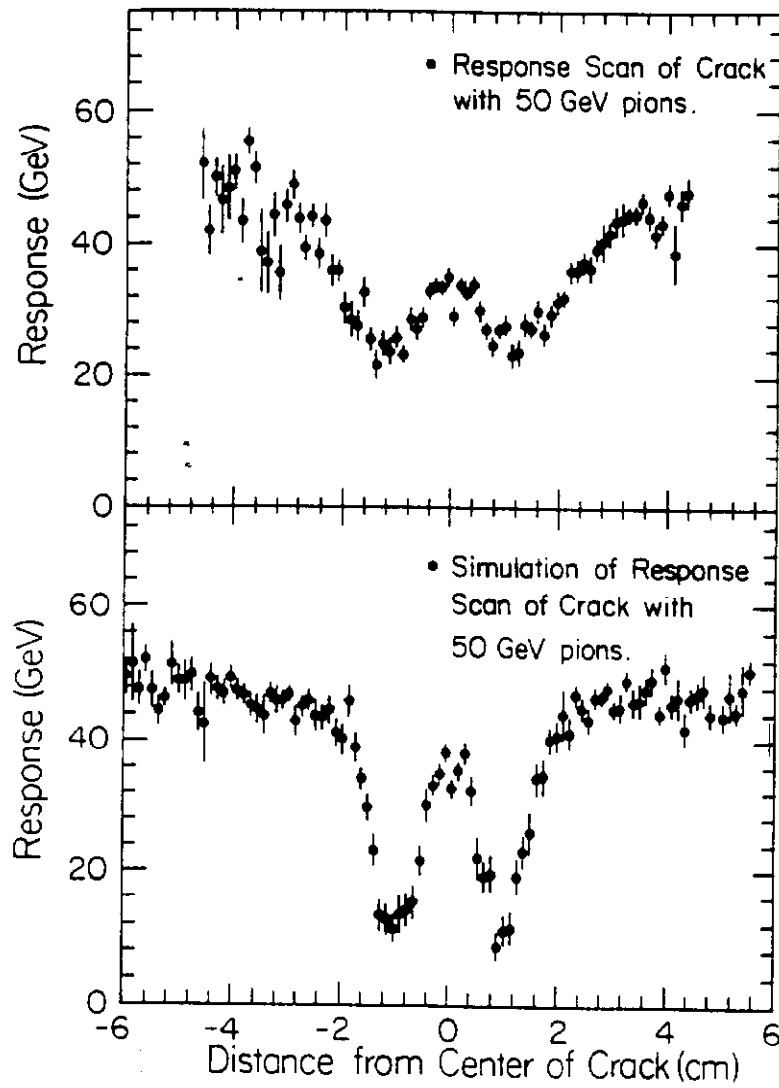
14

Figure 10: Response of the calorimeter to 50 GeV pions scanned across a $\phi$ crack in the central calorimeter. The lower figure shows the response in the simulation. Although the simulation and the test beam data do not agree in the shape of the response, the average response has been tuned to agree.
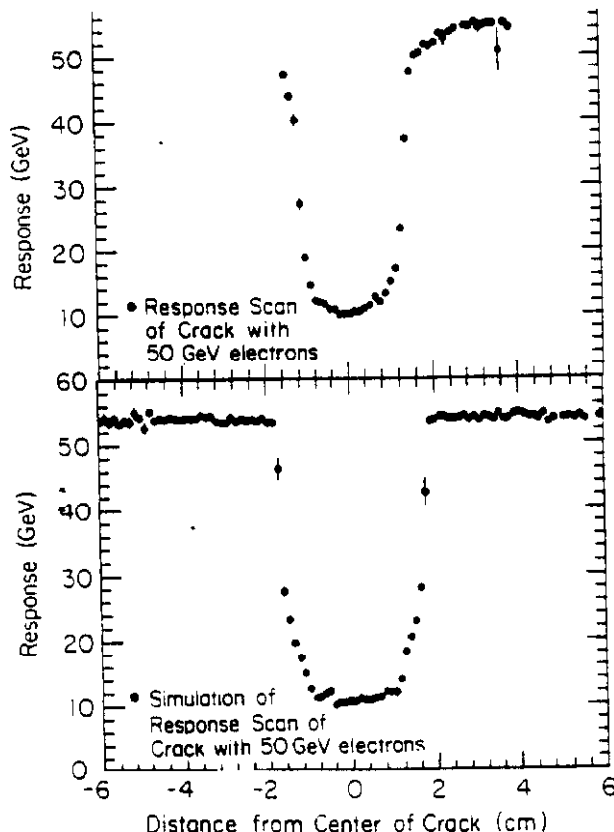
Figure 11: Calorimeter response to 50 GeV electrons scanned across a $\phi$ crack. The lower curve shows the response in the simulation.

### 5.3.2 $\eta$ Cracks

Boundaries between different calorimeters (*eg* plug and central), as well as the gap between the two central calorimeter arches produce cracks in $\eta$. We have attempted to measure the response of the detector to jets in the $\eta$ transition regions using a technique of dijet balancing. The dijet balancing technique was used by the UA2 collaboration [11] to determine jet energy resolution. The technique is based on the premise that typical QCD two jet events in $\bar{p}p$ collisions will approximately balance in $E_t$.

To perform this measurement, we select a *trigger* jet in a uniform region of the central calorimeter, and allow the second jet, or *probe* in the event to fall anywhere else in the detector. By examining the energy imbalance in other regions of the detector, we get a measure of the energy loss in the various crack regions. Figure 12 shows the $E_t$ imbalance in the detector as a function of the $\eta$ of the probe jet. Clearly one can see significant losses at $\eta \approx 0$, 1.2, and 2.4. These correspond to the gaps between the two halves of the central arches, the plug-central boundary and the plug-forward boundary. The detector simulation provides a reliable reproduction of this
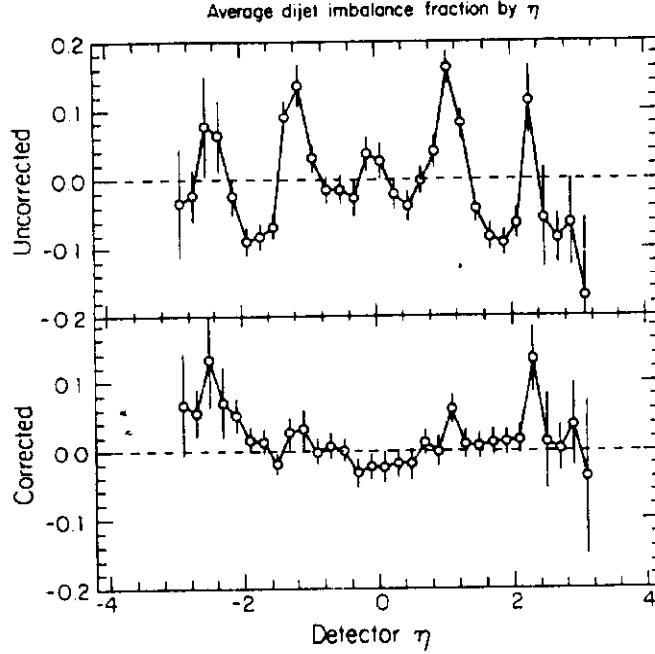
16

Figure 12: The $E_t$ imbalance found from dijet events for trigger jets selected in the central detector and the probe jet allowed anywhere in the detector. Part a shows the imbalance distribution for all jets, and part b shows the same distribution after correcting for known crack losses via simulation.

data. From the detector simulation, we can derive a set of correction factors for jets in the different fiducial regions, and redo the dijet balancing with these corrections. The result is shown in figure 12. Clearly the situation is substantially improved; an imbalance of order 20% goes to about 3% on average. Note that this correction cannot gain back lost resolution.

For a physics analysis where missing $E_t$ is important, it is possible to cut on events which show a significant amount of jet activity near the $\eta$ cracks, and minimize the effects of uninstrumented regions. One improvement in the test beam program would be to build mock-ups of the $\eta$ crack regions and do scans of electrons and pions across the cracks, rather than relying on jet balancing data.

## 5.4 Clustering effects and Underlying event

The corrections due to clustering effects and the underlying event are taken from the data. The underlying event is the energy is associated with the interaction between partons not participating in the hard scattering process; this is azimuthally symmetric, and has a flat rapidity distribution. The

17

clustering corrections take into account the low energy component of jets and include the effect of having a finite energy threshold for towers to be added into the cluster, and also for the energy appearing outside of the clustering cone.

Rather than use a Monte Carlo to make these estimates, we have used the data, generating an operational definition of these corrections. This is because event generators in the end are simply tuned on existing data in order to produce underlying event effects.

### 5.4.1 Underlying Event

Figure 13 shows the azimuthal flow of transverse energy relative to a thrust axis found from summed transverse energy triggers. The back to back structure is characteristic of the two jet final states. At 90° from the thrust axis there is a local minimum in the energy. We have taken the energy density in this region to be representative of the average spectator parton contribution to the event. This represents an extra 1 GeV of energy for a clustering cone of 0.7 units of R. This energy density is independent of the energy of the jets in the event, as can be seen in figure 14 .

From this study, the underlying event energy density was found to be 1.0 GeV/rad$^2$ ± 0.3. The uncertainty comes mostly from the systematic contribution on varying the cuts on third jets for events on the study and the single tower threshold. This translates into a correction of 1.52 ± 0.52 GeV $E_t$ for the clustering cone size.

### 5.4.2 Cluster corrections

The correction for the finite tower threshold was determined by varying the single tower threshold in jet events and looking at the change in cluster energy associated with this cut. The energy appeared to have a well behaved asymptote, indicating that 0.35 GeV should be added in to compensate for this.

The correction for energy outside of the jet cone was determined in a similar way by varying the cone size and looking at the change in energy. Again, a well defined limit appeared to exist, which is illustrated by the cross hatched area in figure 13 . This correction was to add approximately
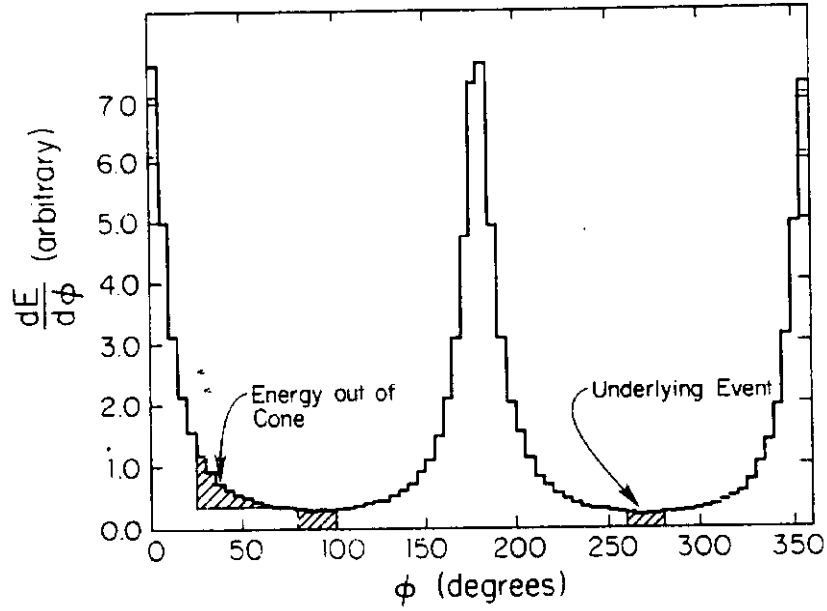
18

Figure 13: Transverse energy deposited in the central calorimeter as a function of the azimuthal angle from the event thrust axis. The minimum at 90° is taken to be the energy from the underlying event. The cross hatched region at 40° would be roughly the amount of energy lost outside of the clustering cone.
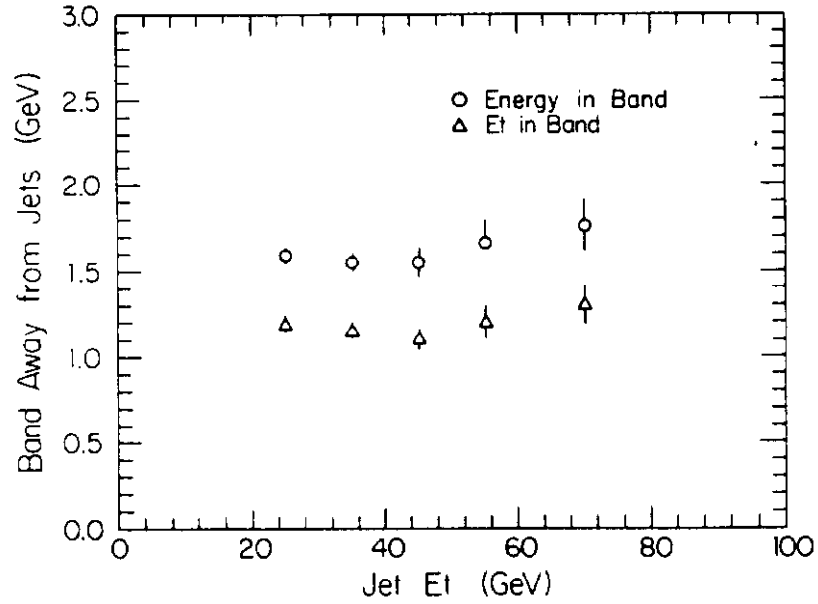


Figure 14: The dependence of the underlying event energy on the $E_t$ of the leading jet.

1 GeV to the jet energy, but is dependent on the size of the clustering cone.

Combining the underlying event and the clustering corrections, we find a correction that adds 0.74 GeV to the jet $E_t$, with a systematic error that is 1.0 GeV. The systematic comes from adding together the uncertainties for each contribution in quadrature. Because the effect of the clustering corrections is to add energy, and the correction for the underlying event is to subtract energy, the systematic error turns out to be larger than the actual correction. There is some question as to whether one should really make a correction for the energy which falls outside of the clustering cone [12]. This is because a QCD calculation made at higher order could, in principle, take this into account, and a correction would really be a double counting. Given the small size of the correction compared to the uncertainty from other effects, it is mostly an academic question at present.

## 5.5   Full Correction and Associated Uncertainty

A full jet energy correction is derived, starting with the tuned version of ISAJET, and the detector simulation with the nonlinearities and the crack response put in properly. The technique using the Monte Carlo is to simulate only the jet part of the event, and turn off the underlying event simulation (which we correct for using the above prescription). The simulated event is divided into hemispheres, and the jet is defined using the final state particles (including neutrinos and muons) produced by the ISAJET partons going into either hemisphere. There is a good reason to use the final state particles rather than the partons in the generator to define the corrections. This is because there is a substantial smearing between the ISAJET parton energies and the final jet energies (ie all the final state particles, including neutrinos that make up the jet). This is because ISAJET rescales all the energies of particles in an effort to conserve momentum and $\hat{s}$ in the event as a whole, which is a reflection of the fact that partons are massless objects, whereas jets have a finite mass associated with them. As a consequence, there is not a good correspondence between the jet energies and the parton energies. This is in general true for most simulations of jets.

The correction factor is derived for the calorimetry effects using the above prescription, and the clustering and underlying event effects are put in after the correction. The correction was parameterized by a spline fit. The result
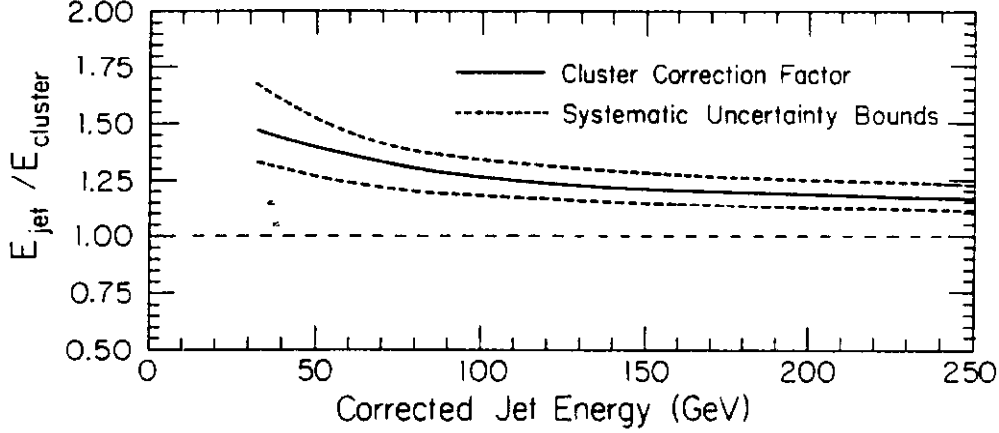
20

Figure 15: Jet energy correction expressed as a ratio of corrected to uncorrected jet energies. The curve is the result of a spline fit to the simulation results. The dashed lines represent the limit of the systematic uncertainty assigned to the correction.

of this procedure is shown in figure 15, with both the data points, and the result of the spline fit. As one can see, at low energies there is a substantial correction, of up to 35%. At the higher energies, the correction is of order 20%. A large fraction of this correction comes from the nonlinearity convolved with the jet fragmentation function, but some component comes from the crack losses.

The systematic uncertainty in the jet energy response is shown in figure 16, broken down into a number of components. Several of the components scale with energy, namely the nonlinearity and the fragmentation uncertainty. The clustering effects, because they are independent of the jet $E_t$, also are less important at larger jet $E_t$'s. The contribution of the uncertainties in the crack response, the calibration and uncertainty in the charge to neutral fraction are roughly constant as a function of $E_t$.

One can conclude from this analysis that the effects of having a non-compensating calorimeter can be managed in most physics analyses. The
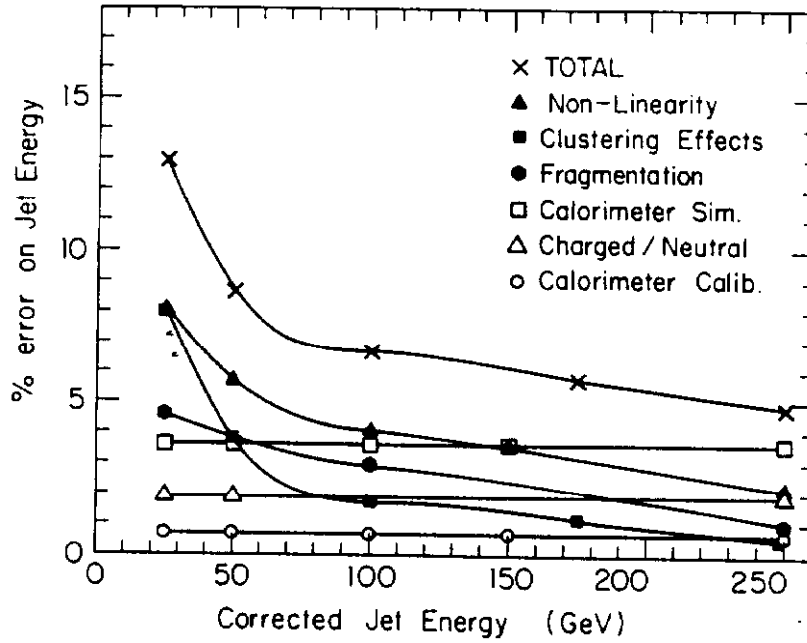
21

Figure 16: The systematic uncertainty in jet energy. Both the total and the contribution from various sources are shown.

nonlinear response to pions generates uncertainties in the response to low energy jets. This uncertainty is dominant for jets with transverse energies below 150 GeV. Above these energies, the simulation of the cracks becomes important.

## 6  Direct Photon $E_t$ Balancing

It is possible to verify the above corrections to the jet energies by using a sample of direct photons. The direct photon Feynman graphs are shown in figure 17. These have jets recoiling against photons in the final state. Because the photon is a localized, purely electromagnetic shower, it doesn't have the uncertainties associated with nonlinearities, and crack response that jets would otherwise have. Even if the direct *photon* is really a single, isolated neutral pion, the point is the same, provided the opening angle of the photons is small compared with the transverse segmentation of the calorimeter. Because the final state should balance in transverse energy, it is possible to use the photon as a calibrated energy source to measure the recoil system
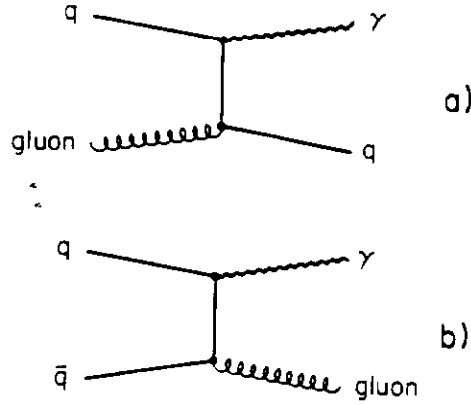
Figure 17: Leading order Feynman diagrams for direct photon production.

independently.

This technique is, in principle also applicable to SSC experiments, and could be considered as a calibration check. If the calorimeter corrections are done properly for the jets recoiling off of photons, the ratio $E_\gamma/E_{jet}$ should have a mean of 1. Figure 18 shows three such balancing plots, for photon $E_t$'s between 10 and 30 GeV. The first and second contain uncorrected jet energies taken with slightly different clustering parameters. The first plot takes a seed tower threshold of 2.0 GeV, and the spike at 0 comes from jets that weren't reconstructed. The second plot has the seed tower threshold set to 1.0 GeV, and the spike has vanished, indicating that this is a more efficient seed threshold for finding jets (particularly low energy jets). The third plot shows the balance when the jet is corrected as described above. The mean of the distribution in which the jet energy is corrected is 1.05, indicating that the corrections are not far off. It is speculated that the high tail of the distribution may be due to radiative processes.
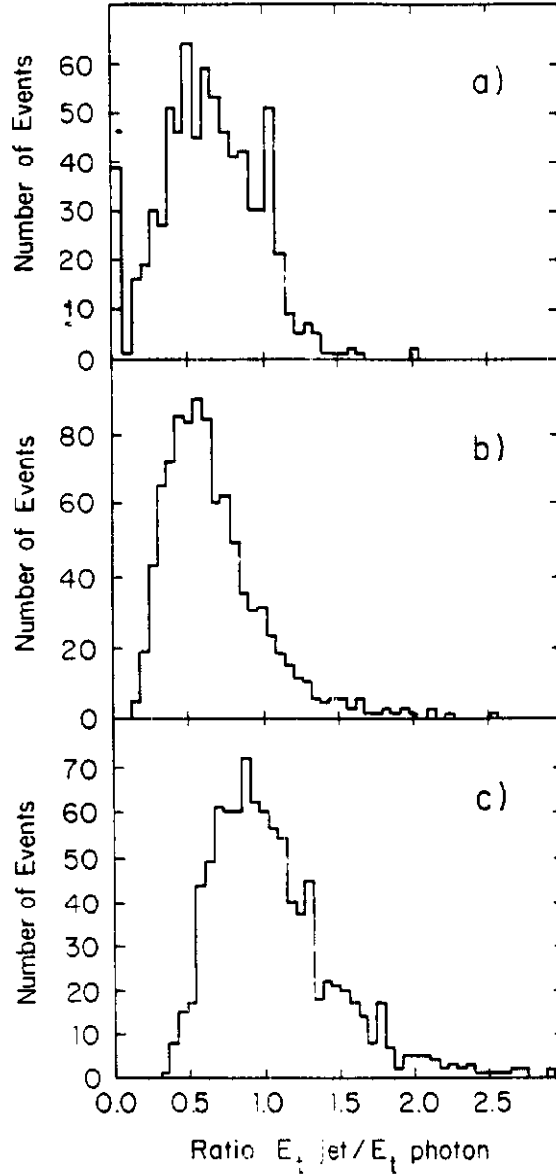
23

Figure 18: Distributions of $E_\gamma/E_{jet}$ for recoiling jets under different conditions. The first is uncorrected jet energies with a seed tower threshold of 2.0 GeV. The second has a seed tower threshold of 1.0 GeV, and the third is correcting the jets in the second plot for known calorimeter effects. The third has a mean of 1.05.

# 7　Smearing

The observed jet $E_t$ spectrum will be a convolution of the finite jet resolution function with a steeply falling spectrum.

$$\frac{d\sigma}{dE_t}\bigg|_{obs} = \int_0^{E_{beam}} G(E_t - E_t')\frac{d\sigma}{dE_t'}\bigg|_{true} dE_t' \qquad (4)$$

where $E_t'$ is the true parton energy, $E_t$ is the measured jet energy, and $G(E_t - E_t')$ is the resolution function. These two effects will steepen the measured spectrum.

The jet $E_t$ resolution is measured by looking at the dijet imbalance in the transverse plane. There are two vectors that we define for this imbalance technique, we will call them $\vec{K_{t\perp}}$ and $\vec{K_{t\|}}$. Figure 19 shows the relation to these vectors to the transverse momenta of the two leading jets. $\vec{K_{t\perp}}$ bisects the angle between the jet momenta, and has an error that can be determined from the average jet $E_t$ and the positions of the jets, which can be measured with a precision of better than 3°, and does not involve the jet energy resolution directly. This component is dominated by QCD effects which give the jets a finite boost in the transverse plane. The intrinsic transverse momentum of the quarks in the proton also give a boost in the transverse plane, but this is substantially smaller than the QCD effects. $\vec{K_{t\|}}$ is perpendicular to $\vec{K_{t\perp}}$ and is a combination of the QCD boost, and the detector resolution. By assuming that the $\vec{K_{t\|}}$ is really a superposition of the QCD transverse boost, and the momentum resolution, we can obtain the resolution by subtracting the two in quadrature,

$$\sigma = \sqrt{|K_{t\|}|^2 - |K_{t\perp}|^2} \qquad (5)$$

Figure 20 shows the value of $\vec{K_{t\|}}$ for different bins of jet $E_t$. Both quantities have no long non-Gaussian tails associated with them.

The jet $E_t$ resolution is approximately 9 GeV for 50 GeV jets. From the measured resolution function from the dijet balancing, and from the measured jet $E_t$ spectrum, we performed a numerical deconvolution to derive the correction factors as a function of jet $E_t$. The ratio of the uncorrected to the corrected cross sections are 1.7 at 30 GeV, and 1.1 at 250 GeV, with a 25% systematic uncertainty at low energy and a 5% uncertainty at high energy.
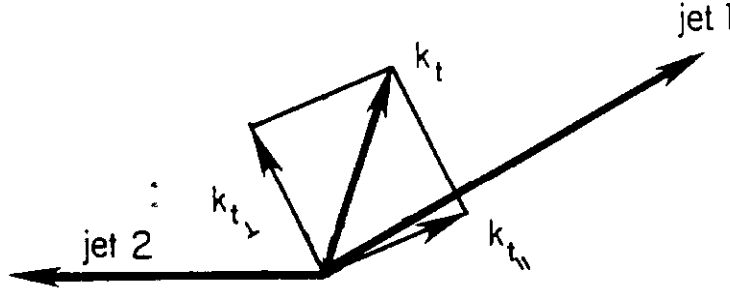
25

Figure 19: The dijet momentum imbalance resolved into two components, $\vec{K}_{t\perp}$ and $\vec{K}_{t\parallel}$. The component perpendicular to the jet axis is dominated by QCD effects, as the angles of the jets can be measured well, the parallel component contains both the QCD smearing and the detector resolution.

## 7.1 Compensation with tracking

It is possible to use tracking information to regain some of the resolution lost because differences in jet fragmentation can lead to a further smearing of the resolution from the ideal single pion response. This occurs because of the low energy response. For example, a jet composed of 100 1 GeV pions will have a different response than a jet composed of 1 100 GeV pion.

In this study, the $E_t$ resolution was taken from a sample of central-central jets. The technique was the same as for the dijet balancing described above. In addition, we computed a missing energy distribution from the jets alone. We computed the $E_t$ resolution in two ways. In the first way, the average corrected jet energy was used. In the second way, the jet energy was first corrected for the known non-linear response for all reconstructed charged tracks pointing at the calorimeter. Then the remaining effects, cracks underlying event were corrected with a residual correction.

In both cases the corrected jet energies had the same mean value. The resolution for jets without the tracking correction was:
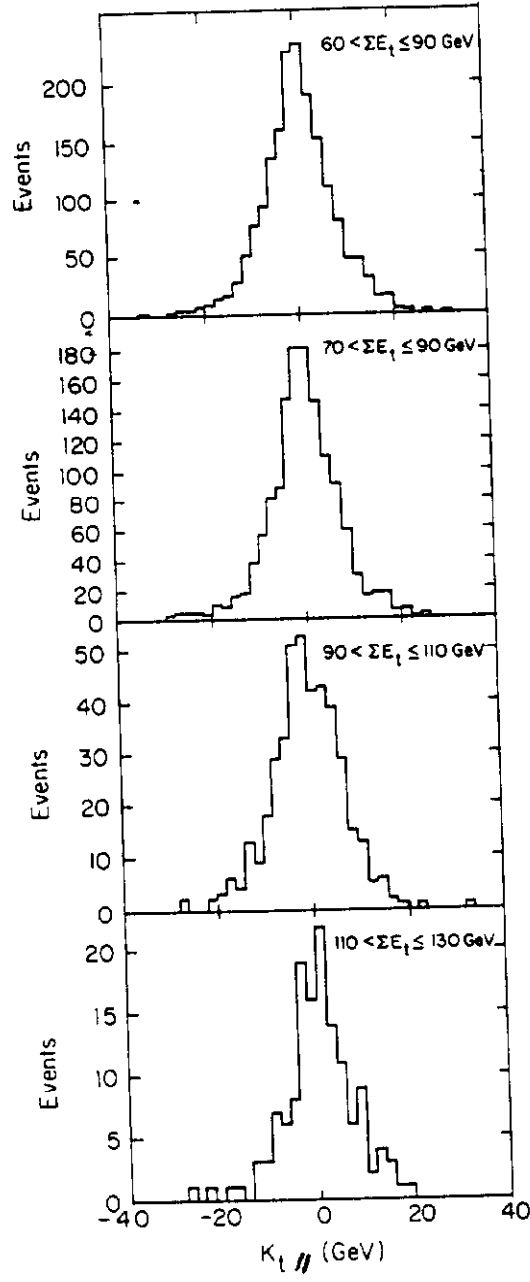
$$\sigma = 1.2\sqrt{E_t} - 3.3 \ GeV \tag{6}$$

Figure 20: The quantity $|K_{t\parallel}|$ plotted for different jet $E_t$ bins. Note the absence of long tails.

In the case where the tracking correction was applied, the resolution was:

$$\sigma = 0.88\sqrt{E_t} - 0.85 \ GeV \tag{7}$$

Clearly the tracking correction improves the resolution, and decreases the effective constant term in the resolution as well. This result perhaps should be expected [7].

# 8  The jet $E_t$ spectrum

After applying all of the corrections, the jet $E_t$ spectrum is formed. Only central jets with $|\eta| \leq 0.7$ were taken in this analysis. The systematic uncertainty in the energy scale is factored into an effective uncertainty in the cross section by error propagation. The local slope of the $E_t$ spectrum is used to convert the energy scale uncertainty into an effective uncertainty in the jet cross section. This uncertainty varies from 45% overall to 70%, and is dominated by the uncertainty in the energy scale. Figure 2) shows the cross section, along with the predictions of leading order QCD, and the effective of contact terms in the Lagrangian with different $\Lambda_c$ values. The uncertainty is a combination of statistical and systematic effects, with the overall normalization uncertainty plotted separately. Only the $E_t$ dependent part of the systematic uncertainty is plotted along with the data points.

From the analysis of 25 nb$^{-1}$ of data taken in 1987, a lower limit on $\Lambda_c$ of 700 $GeV$ was set (95% CL) [15]. From the data being taken in the current run (1988-1989), the detector should be sensitive to compositeness scales of order 1.2 TeV.

# 9  Conclusions

Much experience has been gained in the CDF detector for measuring jets in calorimeters with a projective geometry, including effects such as cracks, lack of compensation *etc* . These effects can be dealt with in a straightforward manner, and reliable corrections and estimates of systematic uncertainties can be derived. Although cracks and non-compensation do generate uncertainties, they do not prohibit physics analyses. Future work on calorimeters
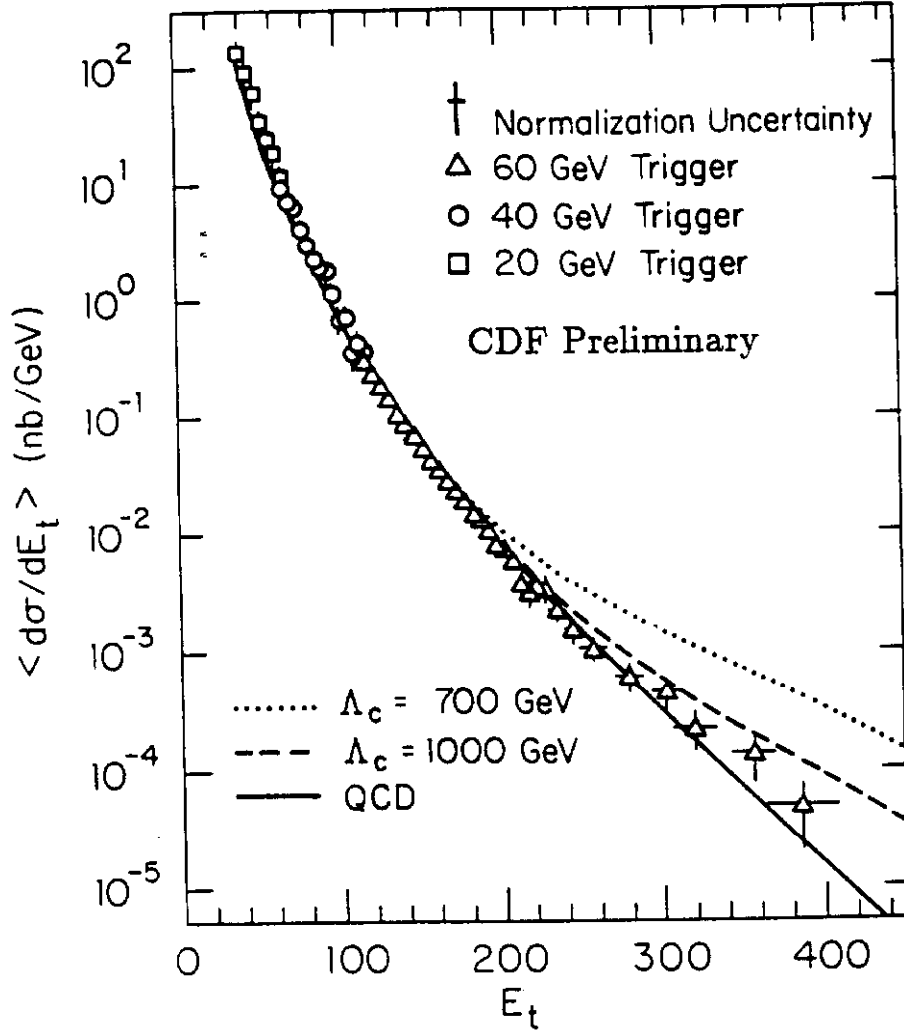
Figure 21: Inclusive jet cross section from 1.4 pb$^{-1}$ from 1988 data taken with the CDF detector. Data are corrected for the effects described in the text. Also plotted are the predictions of leading order QCD (Duke+Owens structure function set II, $Q^2 = 0.5E_t^2$ [14]), and QCD modified by compositeness terms with the characteristic energy scales $\Lambda_c = 0.7$ TeV, and 1.0 TeV.

would be well advised to seek out test beams with the capability of running at low energies, and to scan fully crack regions. *In Situ* calibration checks, such as direct photon data should also be considered.

## 10 Acknowledgements

The work on systematics presented here was performed by the CDF jet/QCD group. Some of the people who contributed to the work shown here include: Steve Kuhlmann, Steve Behrends, Bradley Hubbard, David Brown, Robert Carey, Robert Harris, Simone Del Agnello, Marjorie Shapiro, Brenna Flaugher, Shinhong Kim, Giovanni Punzi, and Robert Blair.

## References

[1] CDF collaboration, Nucl. Instr. and Meth. **A267** 249, 257, 272, 280, 301, 315, 330; **A268** 24, 33, 41, 46, 50, 75 92 (1988).

[2] L. Balka *et al* , NIM, **A267** 272 (1988).

[3] E. Eichten, K. Lane and M. Peskin, Phys. Rev. Lett. **50**, 811 (1983).

[4] P. Frampton, and S. Glashow, Phys. Rev. Lett., **21** 2168 (1987).

[5] G. Sterman and S. Weinberg, Phys. Rev. Lett. **39**, 1436 (1977).

[6] S. Ellis, Z. Kunzst, and D. Soper, Oregon Preprint OITS 395 and 396 (1988).

[7] R. Wigmans, Nucl. Instr. and Meth., **A259** 389 (1987).

[8] F. Paige and S. Protopopescu, in Proceedings of the 1986 Summer Study on the Physics of the Superconducting Supercollider, ed. R. Donaldson and J. Marx, 23 June - 11 July 1986.

[9] P. Ghez, UA1 PhD thesis (unpublished), Universite Scientifique et Medicale de Grenoble (1986).

[10] R. Brandelik, *et. al.* , Phys. Lett. **94B** , 437 (1980).

[11] P. Bagnaia *et al* , Phys. Lett. **144B** , 283 (1984).

[12] D. Soper, Univ. of Oregon, Eugene, personal communication.

[13] R.D. Field and R.P. Feynman, Nucl. Phys. **B136** 1 (1978).

[14] D.W. Duke and J.F. Owens, Phys. Rev. **D30** 49 (1984).

[15] F. Abe *et. al.* , Phys. Rev. Lett., **62** 613 (1989).